

# Unravelling the role of cosmic velocity field in dark matter halo mass function using deep learning

Saba Etezad-Razavi <sup>1</sup>, Erfan Abbasgholinejad <sup>1</sup>, Mohammad-Hadi Sotoudeh <sup>1,2,3</sup>, Farbod Hassani <sup>4</sup>, Sadegh Raeisi <sup>1</sup>, and Shant Baghran <sup>1</sup> 

<sup>1</sup>Department of Physics, Sharif University of Technology, Tehran 11155-9161, Iran

<sup>2</sup>Department of Physics, Université de Montréal, Montréal, Canada

<sup>3</sup>Mila - Quebec Artificial Intelligence Institute, Montréal, Canada

<sup>4</sup>Institute of Theoretical Astrophysics, University of Oslo, 0315 Oslo, Norway.

Accepted XXX. Received YYY; in original form ZZZ

## ABSTRACT

We discuss an implementation of a deep learning framework to gain insight into the dark matter structure formation. We investigate the impact of velocity and density field information on the construction of halo mass function through cosmological  $N$ -body simulations. In this direction, we train a Convolutional Neural Network (CNN) on the initial snapshot of an only dark matter simulation to predict the halo mass that individual particles fall into at  $z = 0$ , in the halo mass range of  $10.5 < \log(M/M_\odot) < 14$ . Our results show a negligible improvement from including the velocity in addition to the density information when considering simulations based on the standard model of cosmology ( $\Lambda$ CDM) with the amplitude of initial scalar perturbations  $A_s = 2 \times 10^{-9}$ . In order to investigate the ellipsoidal collapse models and to study the effect of velocity in smaller mass ranges, we increase the initial power spectrum such that we see the effect of velocities in larger halos which are in the resolution of our simulation. The CNN model trained on the simulation snapshots with large  $A_s$  shows a considerable improvement in the halo mass prediction when adding the velocity field information. Eventually, for the simulation with  $A_s = 8 \times 10^{-8}$ , the model trained with only density information shows at least 80% increase in the mean squared error relative to the model with both velocity and density information at almost all mass scales, which indicates the failure of the density-only model to predict the halo masses in this case. Our results indicate that the effect of velocity field on the halo collapse is scale-dependent with a negligible effect for the standard model of cosmology in mass scales  $10.5 < \log(M/M_\odot) < 14$ .

**Key words:** large-scale structure of Universe – dark matter – methods: statistical

## 1 INTRODUCTION

The standard model of cosmology known as  $\Lambda$ CDM (cosmological constant plus cold dark matter) is established in the last two decades through observation of the cosmic microwave background radiation (CMB) (Aghanim et al. 2020) and large scale structure (LSS) surveys (Percival et al. 2010; Alam et al. 2017; Camacho et al. 2019). Despite many successes of this model in describing the evolution of the Universe, and the statistical distribution of structures, the nature of dark energy, dark matter (DM) and the physics of the early Universe is still unknown. The future LSS surveys, for example, the Vera Rubin observatory, Euclid satellite, and Nancy Groce Roman mission are planned to map the Universe in more detail over a wider

range of redshifts (Rhodes et al. 2019). Accordingly, the study of LSS in the Universe employing high precision  $N$ -body simulations becomes crucial, especially to compare different models against precise observational data.

In the standard picture of structure formation, the galaxies, group of galaxies and galaxy clusters reside in DM halos (White & Rees 1978). These DM halos are the nodes of the cosmic web, which are structured by hierarchical formation. In this sense, the study of DM halo formation is essential for understanding galaxy formation, evolution, and testing our cosmological models. The evolution of DM halos from an initial condition to the late time structures is a complicated non-linear process based on gravitational instability, mainly through mass accretion and mergers of DM structures (Peebles 1980). Also, the knowledge of complicated baryon physics becomes essential to populate DM halos. In this direction cos-

\* baghran@sharif.edu

mological  $N$ -body simulations are used to model these non-linear processes (Springel et al. 2001, 2005; Kuhlen et al. 2012). On the other hand, the analytical models can give insights into the process of structure formation. One of the old but enlightened ideas of these models of structure formation is related to the nominal work of Press and Schechter (PS) (Press & Schechter 1974). They propose that by looking at the statistics of the density field in higher redshifts, where the perturbations are almost Gaussian and linear, we can predict the resulting halo mass function by linear evolution of the density contrast field to the late time. This raises the question that what are the main features of the early Universe which are important to predict the DM halo mass function. The two ideas of peak theory (Bardeen et al. 1986) and excursion set theory (EST) (Bond et al. 1991) are theoretical developments to use the idea of using initial conditions to predict the late time distribution of matter. The two main features of these analytical models are the collapse model (spherical collapse, ellipsoidal collapse (Sheth et al. 2001; Sheth & Tormen 2002)) and the smoothing functions of the initial density field (Nikakhtar et al. 2018).

It is worth mentioning, that due to the enormous amount of data going to be delivered in near future from the cosmological surveys and simulations, we have already entered an era of big data in cosmology. Thus, the Machine Learning (ML) techniques become a complementary way to study the LSS of the Universe (He et al. 2019). ML can be used to have a more precise prediction for the LSS observables and to shed light on the physics and process of structure formation (Lucie-Smith et al. 2019, 2020).

In this work, we use the ML methods to investigate the proposition of the analytical models of structure formation in predicting the late time distribution of the matter. Mainly, we investigate the ideas of spherical collapse and ellipsoidal collapse. The first one is related to the initial smoothed density and the second one incorporate the physics of velocity field and tidal shear of the collapse region. We use the Convolutional Neural Networks (CNN) to study the effect of density contrast and velocity field in LSS formation. The organisation of the paper is as follows: In section 2 we review the theoretical background of this work, in section 3 we discuss the  $N$ -body simulation setups and the data being used in our work, namely we describe our simulations. Section 4 is devoted to the technical description of our method and the deep learning framework. We present our results and interpretations in section 5, and finally, we have our conclusion and future remarks in section 6.

## 2 THEORETICAL BACKGROUND

In the context of the standard model, DM halos are the host of the luminous matter (Press & Schechter 1974; Bond et al. 1991). Accordingly, the statistics and distribution of galaxies are promising tracers of DM distribution in the Universe (Sheth & Tormen 1999). There are two different approaches to study the formation and evolution of DM halos, first through  $N$ -body simulations and second, utilising theoretical ideas to study the mass profile of DM halos. The analytical models are mainly based on the idea of PS (Press & Schechter 1974). In this framework, we study the Universe in high redshift where the perturbations are almost Gaussian and linear. Then, we predict the number density of DM halos by integrating the probability distribution (PDF) of density contrast from the critical density of collapse in spherical model  $\delta_{\text{sc}} \approx 1.69$  to infinity (Press & Schechter 1974). The PDF is constructed using a specific smoothing scale. The mass enclosed in the smoothing region is equal to the mass of the DM halo formed later during the evolution

of the overdense region. Then the two ideas of peak theory (Bardeen et al. 1986) and excursion set theory (Bond et al. 1991) were developed accordingly. An important ingredient of these frameworks is the collapse model. The spherical collapse model (Gunn & Gott 1972) only depends on the value of the over-density in the smoothed scale. However, a more realistic model of ellipsoidal collapse (Sheth & Tormen 2002) indicates the importance of a strong shearing field of velocity which makes the collapse of smaller mass halos more difficult than the larger halo mass. This effect manifests itself in a mass-dependent collapse barrier. To quantify the process we show how the non-linear distribution of DM structures is related to the initial condition. The initial power spectrum of curvature perturbation is defined as

$$\mathcal{P}_{\mathcal{R}} = A_s \left( \frac{k}{k_p} \right)^{n_s-1}, \quad (1)$$

where  $A_s$  is the amplitude of the curvature perturbation,  $n_s$  is the spectral index and  $k_p$  is the pivot wavenumber. The amplitude and the spectral index are fixed by the CMB observations to the values  $A_s \approx 2 \times 10^{-9}$  and  $n_s \approx 0.96$  (Aghanim et al. 2020). We can find the matter power spectrum via the evolution of the scalar Bardeen potential through cosmic time for different modes as (Dodelson 2003)

$$P_m(k, z) = A_l k^{n_s} T^2(k) D^2(z), \quad (2)$$

where  $A_l$  is the late time matter power spectrum amplitude,  $T(k)$  and  $D(z)$  are transfer function and growth function, respectively. The late time amplitude of matter power spectrum is related to initial curvature amplitude as  $A_l = A_s \times (8\pi^2 k_p^{1-n_s}) / (25\Omega_m^2 H_0^4)$ . We can obtain the scale of non-linearity which is a function of redshift and mass using the definition of variance  $S$

$$S(M, z) \equiv \sigma^2(M, z) = \int \frac{dk}{2\pi^2} k^2 P_m(k, z) \bar{W}^2(kR), \quad (3)$$

where  $\bar{W}(kR)$  is the Fourier transfer of the top-hat window function with smoothing scale  $R$  related to the mass scale  $M$ . For the standard cold dark matter model, the variance is a monotonic decreasing function of mass. Larger mass corresponds to lower variance scales. This means that by increasing the variance, we will probe the smaller mass scales. In this work, we increase the primordial curvature perturbation, which results in a higher variance mimicking the small mass range. We will discuss this idea in the simulation section as well. The number density of dark matter halos  $n(M, z)$  can be expressed in terms of variance and the collapse threshold as (Sheth & Tormen 2002)

$$n(M, z) = \frac{\bar{\rho}}{M^2} f(\nu) \frac{d \ln \nu}{d \ln M}, \quad (4)$$

where  $\bar{\rho}$  is the mean density of matter in the present time,  $\nu = (\delta_{\text{sc}}/\sigma(M))^2$  and  $f(\nu)$  is a universal function, related to the first up-crossing statistics in the EST (Nikakhtar & Baghran 2017). For the ellipsoidal collapse the universality function is given

$$\nu f(\nu) = \bar{A} [1 + (\bar{a}\nu)^{-p}] \left( \frac{\bar{a}\nu}{2} \right)^{1/2} \frac{e^{-\bar{a}\nu/2}}{\sqrt{\pi}}, \quad (5)$$

where  $p = 0.3$ ,  $\bar{a} = 0.7$  and  $\bar{A}$  is the normalisation factor. The DM halo number density obtained from the universality function defined in equation 5 is known as the Sheth-Tormen (ST) number density. In the case of  $\bar{a} = 1$  and  $p = 0$  we will find the extended Press-Schechter mass function for spherical collapse (Bond et al. 1991). Note that the ratio of critical density in ellipsoidal collapse

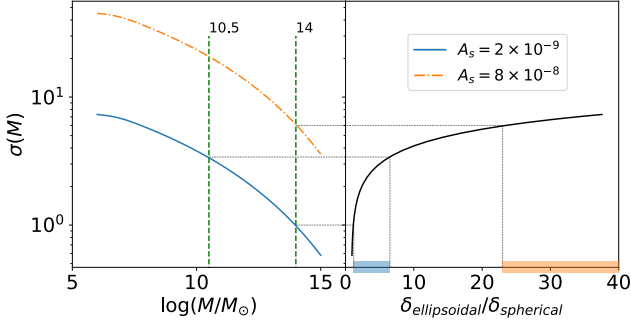


**Figure 1.** The variance of linear matter perturbations is plotted versus mass (left panel) and versus the ratio of critical density of ellipsoidal to spherical (right panel). In the left panel the variance is plotted for two different initial power spectrum amplitude. The green dotted vertical lines shows the scope of the mass range under study.

$\delta_{\text{ell}}$  to spherical collapse  $\delta_{\text{sc}}$  model is defined in ST model as below (Sheth & Tormen 2002):

$$\frac{\delta_{\text{ell}}}{\delta_{\text{sc}}} = \sqrt{\bar{a}} [1 + \beta(\bar{a}\nu)^{-\alpha}], \quad (6)$$

where  $\bar{a} \approx 0.7$ ,  $\alpha \approx 0.615$  and  $\beta \approx 0.485$ . The halo mass function we used in this work for comparison with  $N$ -body simulation data is from Tinker et al. (2008), which calibrate the mass function at  $z = 0$  for virial masses in the range  $10^{11} h^{-1} M_{\odot} \leq M \leq 10^{15} h^{-1} M_{\odot}$  to 5%:

$$\frac{dn}{dM} = f(\sigma) \frac{\bar{\rho}_m}{M} \frac{d \ln \sigma^{-1}}{dM}, \quad (7)$$

where

$$f(\sigma) = A \left[ \left( \frac{\sigma}{b} \right)^{-a} + 1 \right] e^{-c/\sigma^2}, \quad (8)$$

with the fitting functions for constants

$$\begin{aligned} A &= \begin{cases} 0.1(\log \Delta) - 0.05 & \Delta < 1600, \\ 0.26 & \Delta \geq 1600, \end{cases} \\ a &= 1.43 + (\log \Delta - 2.3)^{1.5}, \\ b &= 1.0 + (\log \Delta - 1.6)^{-1.5}, \\ c &= 1.2 + (\log \Delta - 2.35)^{1.6}, \end{aligned} \quad (9)$$

where all logarithms are base 10 and  $\Delta$  is the over-density, where in this work, we set it equal to 200.

To conclude this section, we refer to figure 1, in which we plot the variance of perturbation in terms of DM halo mass in the left panel, for two amplitudes of the initial power spectrum. The vertical dashed green lines show the mass range in our simulation. In the right panel, we plot the variance (same y-axes for both panels) in terms of the ratio of the critical density of ellipsoidal to the spherical model introduced in equation 6. Note that the variance is a monotonic decreasing function of mass, and the critical density ratio is a monotonic increasing function of mass. This is a crucial point to assert that by increasing the amplitude of perturbations for a specific mass range (orange dash-dotted line) we obtain higher variances. It means that by fixing the variance, a mass range in the cosmology with higher initial amplitude corresponds to a smaller mass scale in  $\Lambda$ CDM paradigm, where the velocity shear field is crucial in the collapse model. (Sheth & Tormen 2002; Kameli & Baghran 2020). Accordingly, due to the right panel, we are probing the scales in which the ratio of critical densities are higher than

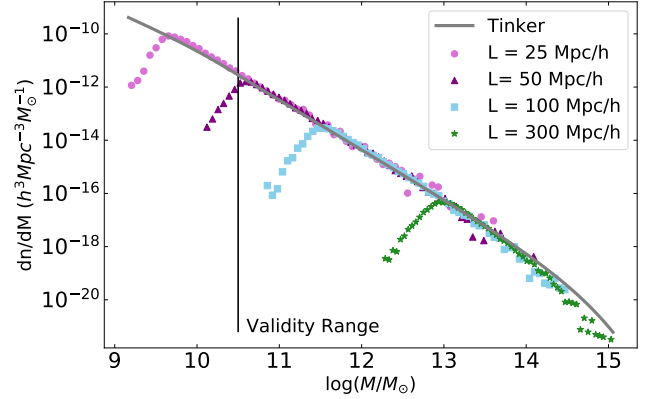


**Figure 2.** Halo mass function for simulation boxes with different sizes and theoretical halo mass function from the Tinker profile is plotted. For box size 50 Mpc/h we have the validity range for halo masses up to 2% in comparison to Tinker profile. This is for the mass range of  $10^{10.5} M_{\odot}$  to  $10^{14} M_{\odot}$ . For all the box sizes, the number of simulating grids is 600, so the number of dark matter particles in the box will be  $600^3$ .

unity. The unity ratio of critical densities means that we have almost spherically collapsed halos, however large ratio indicates that we should consider ellipsoidal collapse, in which the velocities play an important role. This is a key idea in this work, which we will discuss further in upcoming sections.

### 3 N-BODY SIMULATIONS

To study the structure formation using deep learning methods, we use data obtained from gevolution, a relativistic cosmological  $N$ -body simulation (Adamek et al. 2016b,a). In gevolution, the full set of Einstein's equations is solved to update the positions and velocities of particles. One of the main advantages of gevolution is in its natural extendability to consider relativistic particles (e.g., massive neutrinos Adamek et al. (2017)) and to non-standard cosmologies (e.g., different dark energy models and modified gravity theories) (Hassani et al. 2019, 2020; Hassani & Lombriser 2020). The presence of a horizon in relativistic equations compared with the Newtonian ones provides a more accurate analysis of the structure formation at large scales. The gevolution's potential for covering the relativistic particles and seeing their effects in the matter power spectrum on small scales as well as large scales shows us a wide range of exciting possibilities to investigate the effects of non-standard cosmological models (like assuming massive neutrinos or considering different dark energy models) on the perturbation theory and formation of structures in our future works. Assuming the standard model of cosmology,  $\Lambda$ CDM, we run our simulations with a standard cosmological model configuration. Our main training data consists of 10 gevolution boxes with 50 ( $\text{Mpc } h^{-1}$ ) box length and  $600^3$  DM particles within the box. We use the cosmological parameters  $\Omega_{\text{cdm}} h^2 = 0.122$ ,  $\Omega_b h^2 = 0.021$ ,  $T_{\text{CMB}} = 2.725$ ,  $h = 0.67$ ,  $A_s = 2 \times 10^{-9}$ ,  $n_s = 0.96$  and  $N_{\text{eff}} = 3.046$ . We made use of the public halo-finder code Rockstar (Behroozi et al. 2012) to identify halos at  $z = 0$  in the box.

Due to the fixed mesh and finite resolution in our simulation data-sets, there is an inaccuracy in finding small-mass halos. Thus, to find the best mapping between the initial condition of dark matter particles and their final halo mass, we should recognise

the resolution effect on the halo mass function. The resolution limitation is not physical and is only due to the simulation or halo-finder imprecisions. So we have to choose our training data-set from the particles that end up to the halos with proper mass in our specific training box. In order to find the resolution effect, we run four simulations with different resolutions, where the number of particles is fixed to  $600^3$  but different box sizes (25, 50, 100, and 300  $\text{Mpc } h^{-1}$ ) are considered. The overlapped region of the halo mass function for the different resolutions shows the validity range of each simulation. In figure 2 we show the validity range for each simulation. Based on the figure the validity range for the boxsize 50  $\text{Mpc } h^{-1}$ , which is the main simulation being used in this study, within 2% accuracy is  $10^{10.5} M_{\odot}$  to  $10^{14} M_{\odot}$ .

## 4 METHOD: CONVOLUTIONAL NEURAL NETWORK

In this section, we discuss the ML methods we use in this work. In the first subsection 4.1, the convolutional neural network is discussed. In the upcoming subsections, the image construction 4.2, architecture 4.3, loss function 4.4, image size 4.5 and image resolution 4.6 are described respectively.

### 4.1 Convolutional Neural Networks

Convolutional neural networks (CNNs) (Hornik et al. 1987) are one of the most powerful types of neural network models and are widely used for image processing applications. Inspired by Neocognitrons (Fukushima 1980), they benefit from locality-based operations to hierarchically detect translation-invariant patterns and make predictions based on them. Also, they use parameter sharing, which reduces their complexity compared to the traditional neural networks. This allows for building extremely deep neural networks that can learn complex patterns efficiently. From the early applications of CNNs in LeCun et al. (1989) and Lecun et al. (1998) to the modern applications in life sciences (Ramsundar et al. 2019), medical imaging (Lundervold & Lundervold 2019; Yamashita et al. 2018) and autonomous driving (Grigorescu et al. 2020). CNN models have always been one of the driving forces of the field of deep learning.

In recent years, applications of CNNs in cosmology have attracted a lot of attention. This is partly motivated by the big data from cosmological observations and large scale simulations (Siemiginowska et al. 2019). As a more specific example of data-driven cosmology, we follow the line of the research in the LSS, using  $N$ -body simulations as an arena to study the distribution of the matter. For instance, Ravanbakhsh et al. (2017) used a CNN to estimate cosmological parameters directly from zero-redshift density field images and outperformed conventional methods. In Zhang et al. (2019), U-net architecture has been used to infer baryonic matter distribution from less costly dark matter only  $N$ -body simulations. Villaescusa-Navarro et al. (2021) used a CNN model to learn moments of marginalized joint posterior of cosmological and astrophysical parameters, and thereby performed likelihood-free inference to work out  $\Omega_m$  and  $\sigma_8$  from 2D field maps.

Like other deep learning models, CNN-learned feature maps are not easy to interpret. Thus, deriving theoretical conclusions from such models is challenging. Some works have been dedicated to develop methods to interpret neural networks (Ribeiro et al. 2016; Mahendran & Vedaldi 2016; Montavon et al. 2018) or to implement easily interpretable networks (Zhang et al. 2018). It is

also possible to shed some light on deep neural networks by training them using dissimilar or feature-reduced data-sets and comparing the results. For example, Lucie-Smith et al. (2020) tried to interpret the learned feature maps of a CNN to assess the importance of anisotropic features in the prediction of dark matter halo masses. We employed the latter method to draw conclusions from our CNN's trained parameters.

We develop a deep CNN to learn about the physical processes of structure formation directly from  $N$ -body simulations. We train our CNN to learn the halo mass that each particle resides in at the redshift zero. It is worth mentioning that the halo mass is defined based on the number of bound particles, thus there is no assumption on the shape of halos in our analysis. Our CNN's input is the density and velocity field information at  $z = 100$ . We use our trained network to investigate the effect of velocity field in halo collapse and the final halo mass function. In the upcoming subsections, we first describe our data preparation and image construction and then give an overview of the architecture of our CNN model.

### 4.2 Image Construction

We use one of the most basic features of the simulation box, namely the phase space information of the DM particles. We make a 3D cubic image of the local neighbourhood of each particle at the initial snapshot of simulation boxes at  $z = 100$ . Each image consists of the particle itself at the central voxel. We use 0.5  $\text{Mpc } h^{-1}$  comoving size for resolution and an image size of 15 voxels corresponding to 7.5  $\text{Mpc } h^{-1}$  comoving size for our model. We prepare the density and velocity field from the phase space by averaging the information of the particles for each voxel. Images consist of four channels, one for the normalized number of particles in each image pixel and three for the net velocity of particles in the three Cartesian coordinates. We want our model to predict the mass of each particle's final halo destination at the last snapshot  $z = 0$ . For this task, first, we should fix the image resolution and the image size. The combination of 7.5  $\text{Mpc } h^{-1}$  image size and 0.5  $\text{Mpc } h^{-1}$  resolution is the conservative image properties that give us a reasonable run time while preserving the essential information. We will study in more details the choice of these two parameters in the next section after describing our deep learning model and method. The input of our ML model is the image constructed for each particle, and the output is the particle's final destination halo mass.

In order to decrease our machine's sensitivity to different simulation realisations and to reduce the effect of Poisson error, we use 10 independent simulations. Since the number of large halos in the simulation dramatically decreases due to small boxsize and mass resolution consideration, our model may face a sample variance problem as it can not see enough halos at a large mass range. Considering the independent simulations decreases the Poisson error due to the small number of large halos by a factor of one. To reduce it by a larger factor of two, we need 100 independent simulation boxes, which is challenging based on our computational power. We pick 300,000 particles randomly from all these boxes as our training sample. Increasing this number from 300,000 to 400,000 showed minor improvement in the result while adding to the computational cost extensively.

We make the images for each particle in the way described above. We exclude all the particles ending into a halo with masses less than the allowed halo mass range by simulations in both training and testing sets. This choice of minimum halo mass is compatible with our main goal of this work, namely, studying the effect of the velocity field information. Note that the particles ending in cosmic



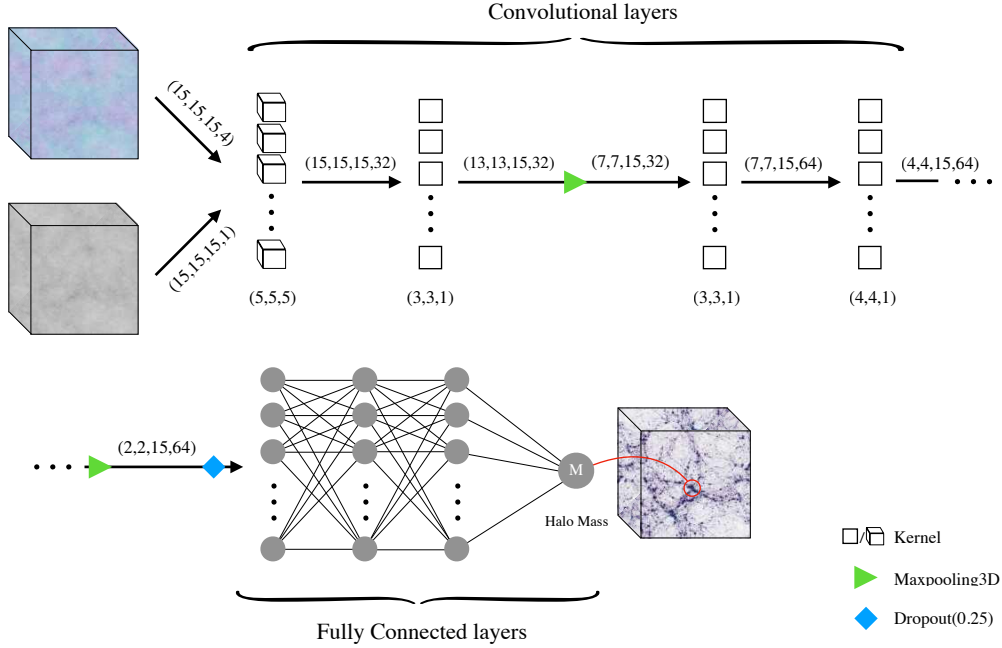


**Figure 3.** We train our CNN on a set of cosmological simulations with different phase space information. Cosmological simulations alone cannot provide us with insight into the physical processes in structure formation and its relation to the main parameters in the initial condition, which are important in halo mass function. We use our neural net, which is trained on different sets of initial condition information of simulation box to provide an understanding of the structure formation. We demonstrated our two kinds of training in this plot. We once train our model on the images with the velocity field information ( $15^3 \times 4$  input shape) and once without ( $15^3 \times 1$  input shape) to investigate the effect of the velocity field in our machinery’s learning.

web structures other than halos such as voids and filaments are not considered in this study; however, they are present in the image of the particles. In fact, one will need a simulation with a larger resolution to broaden the allowed halo mass range for a comprehensive study of structure formation.

Based on the physical properties of structure formation, we expect the inferred halo masses to be invariant under reflection and rotation of the input subregions. In order for our model to meet such symmetries, we use 48 members of the cube symmetry group to replicate our input images. This has been shown to effectively reduce the variance of predictions within the replicates of each subregion in [Ravanbakhsh et al. \(2017\)](#). However, in order to speed up the training process, we do not use the whole replicates to augment our data-set. Instead, during the generation of each mini-batch, each input image is transformed by a randomly selected member of the symmetry group. While preserving the possibility of feeding our model with different transformations of each subregion, this approach considerably reduces our training time.

### 4.3 Architecture

Our model is a deep convolutional neural network which its architecture is described in table 1. The model has two parts: a contracting path and a fully connected component. The contracting path consists of two scales. At each scale, the input is passed through two convolutional layers, followed by a max pooling layer. In each convolutional layer, a set of filters are convolved with the input and the result is passed through an activation function. These operations are used to extract features from the input. Max pooling layers down-sample the feature maps on each scale while preserving their important structural information. This is done by sliding a kernel across each image channel and putting the maximum value of each

Input:		Subregion around a particle		shape: (15, 15, 15, 4)		
layer	type	kernel size	padding	activation	param #	output shape
1	Conv3D	(5, 5, 5)	same	sigmoid	16032	(15, 15, 15, 32)
2	Conv3D	(3, 3, 1)	valid	relu	9248	(13, 13, 15, 32)
3	Maxpooling3D	(2, 2, 1)	same	-	0	(7, 7, 15, 32)
4	Conv3D	(3, 3, 1)	same	relu	18496	(7, 7, 15, 64)
5	Conv3D	(4, 4, 1)	valid	relu	65600	(4, 4, 15, 64)
6	Maxpooling3D	(2, 2, 1)	valid	-	0	(2, 2, 15, 64)
7	Dropout (0.25)	-	-	-	0	(2, 2, 15, 64)
8	Flatten	-	-	-	0	(3840)
9	Dense	-	-	relu	460920	(120)
10	Dense	-	-	relu	7260	(60)
11	Dense	-	-	linear	61	(1)
Output:		Destination halo mass		shape: (1)		

**Table 1.** The architecture of the sequential Convolutional Neural Network model.

resulting region in the corresponding location of the respective output channel. Fully connected layers use the feature maps extracted by the contracting path to infer the scalar value of the halo mass to which the central particle of the input image will finally belong (see figure 3).

### 4.4 Loss Function

The objective loss function used for the model is mean squared error (MSE) which is minimised using the Adam optimisation algorithm ([Kingma & Ba 2017](#)). As we will demonstrate later, our model with this symmetric loss function introduces a systematic error, which causes us to over-estimate the halo mass at smaller mass ranges.

In figure 4, we see an over-prediction for the mass of smaller halos. This feature is present in all samples, indicating an intrinsic error in

the ML method. Accordingly, as the over-prediction increased with a higher minimum mass range, we will not restrict our sample with this consideration. Even more, we use the smaller mass range which is not in the range of our model prediction. This is done in order to transfer the over-prediction error to a smaller mass range which is out of the scope of the study. As demonstrated in figure 4, we can see that changing the minimum halo mass given to the CNN model does not affect the prediction of the model more than the systematic error due to the symmetric loss function that we discussed above. This means that predictions of the halo mass are not affected by slightly changing the minimum used in our training and thus it is independent of our choice of halo mass range in the training set.

#### 4.5 Image size

One of the critical hyperparameters of our model is the physical size of the input images. The initial density contrast field at  $z = 100$  is almost homogeneous and less than unity. Furthermore, for a desired final halo, we can approximate the initial proto-halo (ph) size as  $V_{\text{ph}} = M_{\text{halo}}/\bar{\rho}_i$ , where  $\bar{\rho}_i$  is the average density of the simulation box at  $z = 100$ . As a result, the image size should be at least the volume needed to contain all the most massive halo particles. There is a trade-off in choosing our image size. Our mapping between these images to the halo mass only aims to find the future host halo's mass of the central part of the image. Besides their substantial computational cost, large volume images may mislead the machine when we are not on the density field peaks, and many proto-halo regions exist within a single image. Also, we can not choose our images too small, as we miss some information necessary to find the future halo mass of the specified region in the initial box. We do some scale tests for choosing the best possible image size. We change the image size slightly around the value we obtained as described, and compare our model's performance with different image sizes. Figure 5 indicates that the error due to image size is almost the same for all sizes that we investigate. In general, we can categorise the systematic errors involved in our machinery as a) error due to resolution of the simulation (see figure 2), b) the systematic over-prediction error (see figure 4), and c) error due to the characteristic of the image (figure 5, figure 6). We set an upper limit of 20% for our uncertainty, and for the rest of the work, we choose a specific set of hyperparameters for our images concerning the three sources of error mentioned earlier. This means the minimum mass is set to the minimum halo mass in simulations as described in section 4.4, and the image size is set to  $7.5 \text{ Mpc } h^{-1}$  (15 voxels).

#### 4.6 Image resolution

After fixing the appropriate image size, we specify the image resolution for the CNN input. The volume of the minimum halo mass in the initial condition is the lower bound for the resolution. Thus we pick a value using this minimum bound, and then we change our model's resolution around this specific value to reach the best resolution. As we show in figure 6, increasing the image's resolution by a factor of 1.25 does not change the overall accuracy of the model in the desired mass ranges noticeably. Note that this is done while keeping the physical length of the image constant. However, this increase in the resolution adds to the computational cost more than a factor of two. Furthermore, resolution 100 (physical voxel size of  $0.5 \text{ Mpc } h^{-1}$ ) is a convenient choice.

## 5 RESULTS

We use the basic phase space information of the initial simulation box as the input of our CNN model. We make images of the particle's local neighbourhood and train our machine to predict the mass of the final halo to which this particle ends up from its local neighbourhood picture. We use a training set of 300,000 images randomly chosen from 10 different realisations of the same cosmological parameters. Using the results described in section 4 to fix the hyperparameters of the CNN model, we set the image size to be  $7.5 \text{ Mpc } h^{-1}$  or 15 pixels and with a resolution of  $0.5 \text{ Mpc } h^{-1}$ . Our results can be separated into two main parts. First, we use our model to recover the halo mass function of a completely new box but with the same cosmological parameters as the training boxes in subsection 5.1. Then we present a physical interpretation of the structure formation using our framework based on the effect of velocity in the structure formation in subsection 5.2.

### 5.1 Halo Mass Function Prediction

The aim of constructing an accurate predictor for halo masses is to eventually predict the halo mass function, given an initial distribution of particles. Furthermore, we use the distance of our predicted halo mass function from the real halo mass function as a metric to measure the performance of our model. To predict the halo mass function, we first need to apply a binning on our regression problem and then find the predicted number of halos corresponding to each halo mass bin. As the prediction of halo mass function is strongly dependent on the bin number, we should be careful about our binning definition. We define 40 bins between  $10.5 \leq \log(M/M_{\odot}) \leq 14$  linear in the logarithm of mass. By applying the trained model on a set of 280,000 randomly chosen particles in our test box and predicting the halo mass for each of them, we already acquired the number of particles in each halo mass bin. Next, we use the average density of each halo mass bin to convert the number of particles to the number of halos in that bin. One also must scale this result by the relative ratio of the total number of randomly chosen particles used in this prediction over the total number of particles in the box. The main two contributing factors in the error of this distribution are first, the systematic error in the prediction of halo masses arising from our CNN model's imprecision, and the second error comes from the lack of enough data in chosen random point. Each error is shown in figure 7, where we demonstrated the predicted halo mass function of the box. At our ending mass bins, where the sample variance due to lack of most massive halos increases, our confidence in prediction drops. The colour bar in this plot corresponds to the statistical error with n-sigma deviation of our prediction from the real HMF of the box which is our metric. Our prediction for the HMF is in agreement with the real one from the simulations in the most mass ranges. However, our prediction ability drops considerably for the mass ranges of  $\log(M/M_{\odot}) < 11$ , which is because of the effect we described in section 4. This result shows that our model prediction is trustable the most in the range of  $11 < \log(M/M_{\odot}) < 13$ .

### 5.2 The role of velocity field in structure formation

To investigate the effect of velocity field in the process of dark matter halo formation, we train our model on different sets of input features. One only consists of the density field information, while the other also consists of each particle's velocities in the three Cartesian coordinates. We change our CNN model in each case to fit the input image shape (15,15,15,1) for the case without velocity

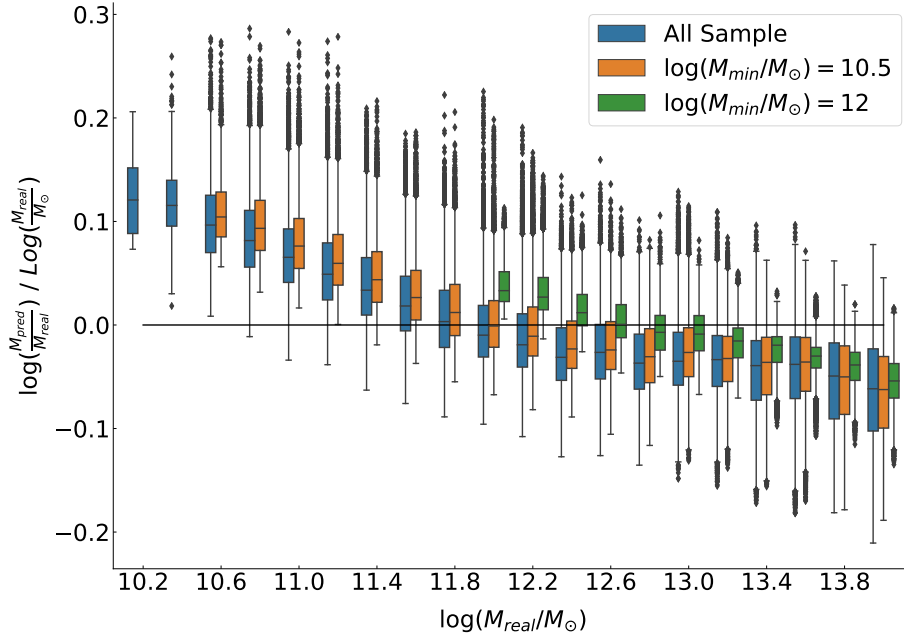


**Figure 4.** The mass of the predicted dark matter halos to the real mass sample is plotted for three minimum mass ranges of the machine entry data. The error bars show the mean and the  $\pm 25\%$  of the distribution. Different colours show the minimum mass which is chosen for ML. The presence of the non-symmetric outliers shows the systematic overprediction of our model at the smallest halo ranges. We resolve this issue by keeping the complete halo mass range of the box while only trusting the results on an interval. This technique pushes the over-prediction to the mass ranges, which are out of the range of interest.

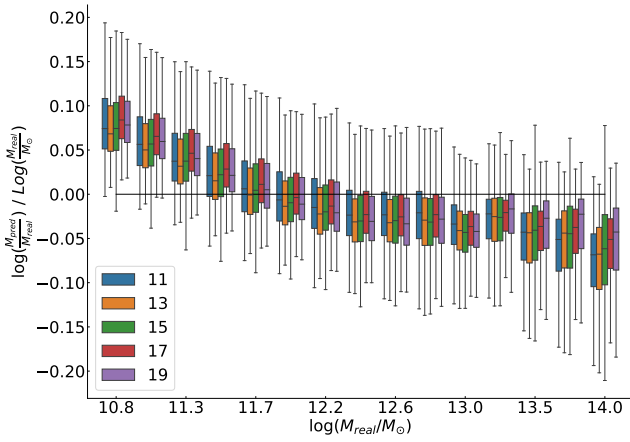


**Figure 5.** The mass of predicted dark matter halo with respect to real one is plotted versus mass for different image size. The different colours correspond to different image sizes in unit of  $\text{Mpc } h^{-1}$ . The error bars shows the  $\pm 25\%$  of the prediction distribution in each mass bin.

information and (15,15,15,4) for when the velocity information is also provided. Except for the first layer, which is changed to fit the input's shape, all the other layer's architecture remains the same. In figure 8, we show the prediction of halo mass with and without considering the velocity information. Violins represent two different sources of error in each halo mass bin. One is the distance of the solid line to the distribution average for predicted halo mass in each mass-bin (the accuracy of the result), and the other is the variance of the distribution for the predicted halo mass (precision of our prediction). To consider these two error sources, we use the R2-score, which would be a reasonable metric to see whether there is an improvement in the prediction with and without velocity in

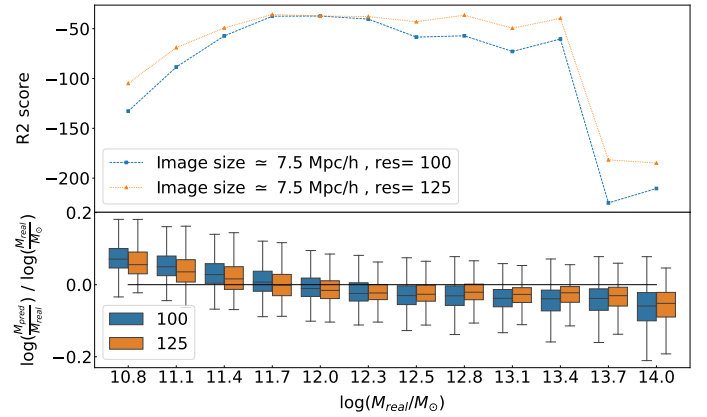


**Figure 6.** The relative error and R2-score of the predicted final halo mass with respect to real one is plotted versus mass for different image resolution of  $100^3$  and  $125^3$  voxels for a  $50 \text{ Mpc } h^{-1}$  box.

each halo mass bin.

The advantage of this metric is that by dividing the model's standard deviation, it measures the score relative to the model itself and thus enables us to compare the score of the two different models. We use R2-score measurement to quantify the performance of our model, where the R2-score is measured in each mass scale as:

$$\text{R2-score}(y_{\text{real}}, y_{\text{pred}}) = 1 - \frac{\sum_i (y_{\text{real}}^{(i)} - y_{\text{pred}}^{(i)})^2}{\sum_i (y_{\text{real}}^{(i)} - \bar{y})^2},$$

where  $y_{\text{real}}^{(i)}$  is the real mass of the particle's destination halo and  $y_{\text{pred}}^{(i)}$  is the prediction of our model for it, and the  $\bar{y}$  is the average

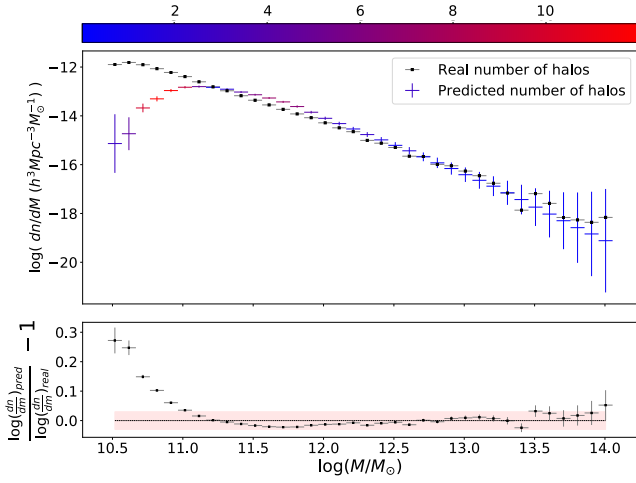


**Figure 7.** The number density of predicted and real dark matter halos plotted versus mass in upper panel. The colour-bar shows the  $\sigma$ -deviation of our predicted model compared to the real data. In the lower panel, we show the ratio of the number density, the shaded region shows the 3% confidence level. In both panels we show the model which consider the velocity as well as density field as an input.

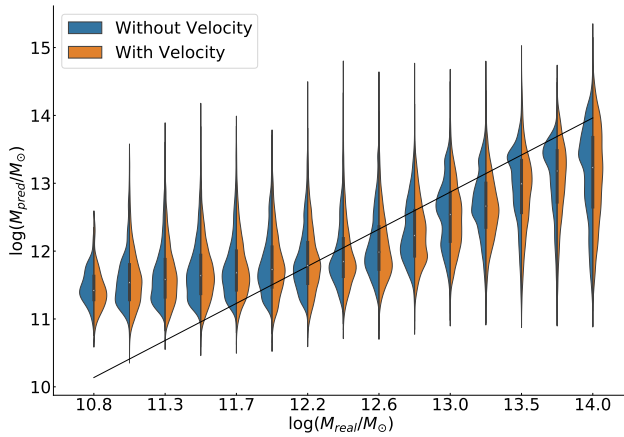


**Figure 8.** The predicted mass of dark matter halos versus the real mass is plotted. The violins show the distribution of our prediction for two different sets of training data with velocity (blue/left) information and the other without velocity (orange/right) information.

$y_{\text{pred}}$  on that mass bin. We measure the R2-score on different mass scales for the two configurations. One with and the other without velocity information in the case of standard initial power amplitude  $A_s = 2 \times 10^{-9}$ .

We use the cross-validation technique to find the error bars on our model. In each case, we train our model five separate times on randomly chosen training sets of the same size. We measure the R2-score for each of these different trained models at each mass scale and use the mean and standard deviation of the bootstrapped sample as our model's mean and uncertainty in terms of the R2-score.

Based on figure 9 the mean R2-score value does not change considerably for the model without velocity in comparison with the one with velocity field information. However, the uncertainty of

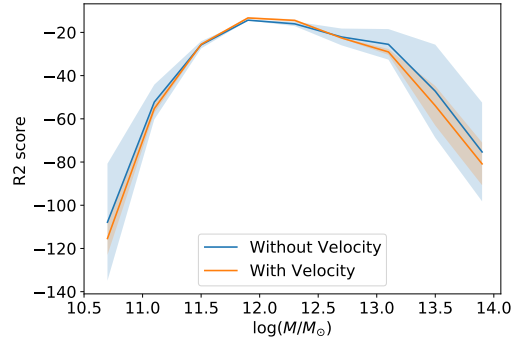


**Figure 9.** R2-score for the two with and without velocity models. The result shows that there is a negligible difference between the performance of these two models in the standard model of cosmology with initial curvature perturbations of  $A_s = 2 \times 10^{-9}$ .

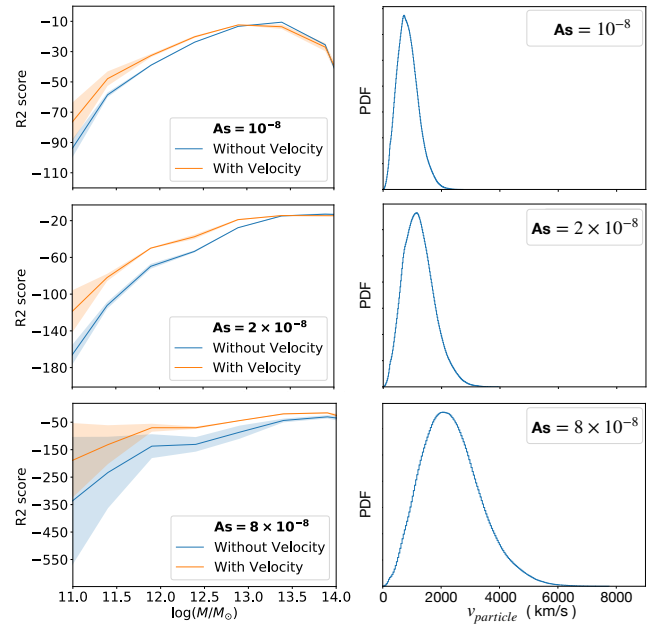


**Figure 10.** The R2-score statistics is plotted versus mass for three different initial power spectrum in the left panel. In the right panel, we show the distribution of dark matter particle's velocity. Right panel indicates that the peak of the velocity distribution of particles moves to larger values when we increase the initial curvature perturbations.

prediction (standard deviation of the bootstrapped sample) reduces for the model with velocity field information. Our result in figure 9, demonstrates that in the mass range  $10.5 \leq \log(M/M_\odot) \leq 14$ , there is no compelling evidence on the importance of velocities in our predictions. However due to our discussion in section 2, we anticipate that the velocities should be important in small mass scales. Nonetheless, due to the mass resolution limitations of our simulations, this regime is not accessible to our current computational power and configuration. To overcome this obstacle, we use an idea to check the velocity dependence of the structure formation. We increase the initial power spectrum of the perturbations in the  $N$ -body simulation runs. This causes that dark matter halos in our simulation mimics the velocity field in smaller mass range halos due to their higher over-density, as discussed in section 2.



Again, we train our model five times for the new set of simulations with a higher initial power spectrum, and we compare the R2-score of bootstrapped cross-validated samples. The result is demonstrated in figure 10. As before, the solid lines are the extrapolation of the mean of the R2-score in each mass bin and the shaded regions are the  $1\sigma$  uncertainty obtained from bootstrap. The right panel in figure 10 indicates that by increasing the initial power spectrum, the distribution of the velocities shifts to higher values. This implies that by increasing the initial power spectrum we can bring the effect of velocity field to larger mass scales which effectively means that by looking at a fixed halo with a specific mass in this non-standard case we are looking at smaller mass dark matter halos compared to the standard model case. The left panel of figure 10 shows that the precision of the model without velocity field drops significantly when the initial power spectrum increases. Moreover, the difference between the model trained with velocity field information and the one without it increases noticeably when increasing the initial power. To show this more explicitly, we measure the difference between the two models for each case. As both models (with and without velocity channels) are trained on the same data-set, the standard deviation in each mass bin is the same. Thus using the mean squared error (MSE) of each model should be sufficient to compare their performances. We measure the relative difference of the two models in each mass bin,  $d(M_{\text{bin}})$ , using:

$$d(M_{\text{bin}}) = \frac{|\text{MSE}_{\text{without}}(M_{\text{bin}}) - \text{MSE}_{\text{with}}(M_{\text{bin}})|}{\text{MSE}_{\text{with}}(M_{\text{bin}})},$$

where,

$$\text{MSE}(M_{\text{bin}}) = \frac{1}{N} \sum_{i=1}^N (M_{\text{pred}}^{(i)} - M_{\text{real}}^{(i)})^2,$$

and  $N$  is the total number of particles on that specific mass bin. Figure 11 shows the result of this distance for different amplitude of initial curvature perturbations, where the errors are obtained from cross-validation. The figure implies that the prediction of model with velocity information is much better than the one without velocity for the large amplitude of initial curvature perturbations. This is consistent with our previous discussion that higher initial amplitudes brings the effect of velocities into larger mass halos compared to the  $\Lambda$ CDM case. This is done by increasing the ratio  $\delta_{\text{ell}}/\delta_{\text{sc}}$  at larger mass halos to mock the effect of velocity shear field which is visible in the small mass halos in the  $\Lambda$ CDM paradigm. As a result, we assert that the velocity information is important in small scales. Our result obtained from a deep learning framework which is independent of collapse model, illustrates that the ellipsoidal collapse model will diverge from the spherical collapse model on small scale in the standard model.

## 6 CONCLUSIONS AND FUTURE REMARKS

We developed an interpretable deep learning framework to shed light on the process of structure formation. We train a CNN model on an initial simulation box at  $z = 100$  to find the final destination halo mass for each DM particle. Our method, in comparison with its previous studies, has the advantage of being simple in terms of the initial features. We use our prediction for the halo mass function as the indicator of the performance of our machinery. Our results in terms of the halo mass function are in agreement with

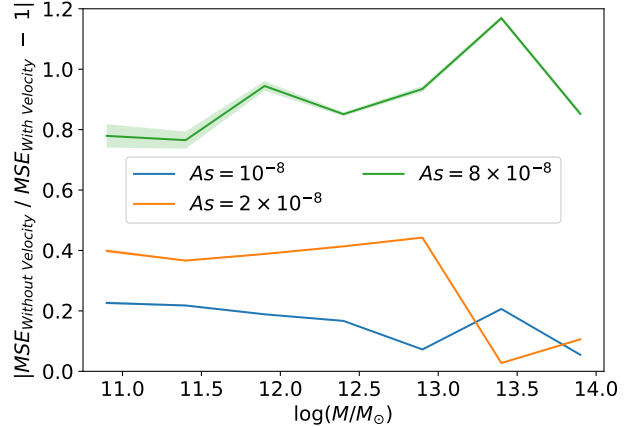


**Figure 11.** The difference between the two (with and without velocity) models for different initial curvature perturbations are plotted versus mass. By increasing the power to  $A_s = 8 \times 10^{-8}$  the difference of two models increases to more than 80%. This implies that for higher  $A_s$  values the density field information is not enough to predict the halo mass function accurately.

the one from the simulation box up to  $1\sigma$  in the halo mass range of  $11 < \log(M/M_{\odot}) < 13$ . We use our framework to find the importance of velocity field in the structure formation process. We train our CNN on two different sets of samples: one the images with velocity channels and the other without velocity channels. Our results imply that the effect of velocity field in the standard model of cosmology given the initial curvature perturbations  $A_s = 2 \times 10^{-9}$  is negligible in the mass range of  $10.5 < \log(M/M_{\odot}) < 14$ . To study the effect of velocity field on smaller scales we use a novel idea. We increase the initial curvature perturbations to increase the variance of perturbations in the scales that are in the scope of our simulation. This causes that massive halos mimic the effect of velocity fields of small mass range. Accordingly, the effect of velocity becomes visible in larger mass halos of our simulations with the given resolution. We observe that increasing the initial curvature perturbations increases the effect of velocity field in the structure formation process in the given halo mass range, correspondingly. This result implies that the effect of velocity field in structure formation is scale-dependent and increases in the smaller mass scales. It is noteworthy that the halo mass, in our analysis, is defined based on the number of bound particles and we do not have any pre-assumptions on the shape of halos. So, there is no constraint on our learning process to select any specific collapse model. Accordingly, our results indicate the full consideration of an ellipsoidal collapse may be essential to reach a more viable halo mass function in small scales, and the simple spherical collapse model would not be sufficient.

Future work might study the correlation between the accuracy in halo mass prediction and the particle's distance from its host halo centre. This is to integrate the idea of peak theory and excursion set theory of peaks in our ML methods. We can use our deep learning method to probe other cosmologies; for example, the models that velocity may play an important role in large mass halo formation. Also, this method can be used to investigate the effect of velocity field on the structure formation in extensions of the standard model (e.g., massive neutrinos) and alternative models (e.g.,  $k$ -essence models).

## ACKNOWLEDGMENTS

This work is supported by Oslo University computational facilities and a grant from the Swiss National Supercomputing Centre (CSCS) under project ID s1051. SB is partially supported by Abdus Salam International Center of Theoretical Physics (ICTP) under the junior associateship scheme. This research is supported by Sharif University of Technology Office of Vice President for Research under Grant No. G960202.

## DATA AVAILABILITY

The simulations data and codes developed in this paper will be provided upon request to the corresponding author. The version of gevolution used in this work is publicly available on: <https://github.com/gevolution-code/gevolution-1.2>

## REFERENCES

- Adamek J., Daverio D., Durrer R., Kunz M., 2016a, *JCAP*, 07, 053
- Adamek J., Daverio D., Durrer R., Kunz M., 2016b, *Nature Phys.*, 12, 346
- Adamek J., Durrer R., Kunz M., 2017, *JCAP*, 11, 004
- Aghanim N., et al., 2020, *Astronomy & Astrophysics*, 641, A6
- Alam S., et al., 2017, *Monthly Notices of the Royal Astronomical Society*, 470, 2617
- Bardeen J. M., Bond J., Kaiser N., Szalay A., 1986, *The Astrophysical Journal*, 304, 15
- Behroozi P. S., Wechsler R. H., Wu H.-Y., 2012, *The Astrophysical Journal*, 762, 109
- Bond J. R., Cole S., Efstathiou G., Kaiser N., 1991, *ApJ*, 379, 440
- Camacho H., et al., 2019, *Monthly Notices of the Royal Astronomical Society*, 487, 3870
- Dodelson S., 2003, *Modern Cosmology*. Academic Press, Amsterdam
- Fukushima K., 1980, *Biological Cybernetics*, 36, 193
- Grigorescu S., Trasnea B., Cocias T., Macesanu G., 2020, *Journal of Field Robotics*, 37, 362
- Gunn J. E., Gott III J. R., 1972, *Astrophys. J.*, 176, 1
- Hassani F., Lombriser L., 2020, *Mon. Not. Roy. Astron. Soc.*, 497, 1885
- Hassani F., Adamek J., Kunz M., Vernizzi F., 2019, *JCAP*, 12, 011
- Hassani F., L'Huillier B., Shafieloo A., Kunz M., Adamek J., 2020, *JCAP*, 04, 039
- He S., Li Y., Feng Y., Ho S., Ravanbakhsh S., Chen W., Poczós B., 2019, *Proc. Nat. Acad. Sci.*, 116, 13825
- Homma T., Atlas L. E., Marks R. J., 1987, in *Proceedings of the 1987 International Conference on Neural Information Processing Systems*. NIPS'87. MIT Press, Cambridge, MA, USA, p. 31–40
- Kameli H., Baghran S., 2020, *Mon. Not. Roy. Astron. Soc.*, 494, 4907
- Kingma D. P., Ba J., 2017, *Adam: A Method for Stochastic Optimization* ([arXiv:1412.6980](https://arxiv.org/abs/1412.6980))
- Kuhlen M., Vogelsberger M., Angulo R., 2012, *arXiv preprint arXiv:1209.5745*
- LeCun Y., Boser B., Denker J. S., Henderson D., Howard R. E., Hubbard W., Jackel L. D., 1989, *Neural Computation*, 1, 541
- Lecun Y., Bottou L., Bengio Y., Haffner P., 1998, *Proceedings of the IEEE*, 86, 2278
- Lucie-Smith L., Peiris H. V., Pontzen A., 2019, *Mon. Not. Roy. Astron. Soc.*, 490, 331
- Lucie-Smith L., Peiris H. V., Pontzen A., Nord B., Thiyaalingam J., 2020, *Deep learning insights into cosmological structure formation* ([arXiv:2011.10577](https://arxiv.org/abs/2011.10577))
- Lundervold A. S., Lundervold A., 2019, *Zeitschrift für Medizinische Physik*, 29, 102
- Mahendran A., Vedaldi A., 2016, *International Journal of Computer Vision*, 120, 233–255
- Montavon G., Samek W., Müller K.-R., 2018, *Digital Signal Processing*, 73, 1
- Nikakhtar F., Baghran S., 2017, *Phys. Rev. D*, 96, 043524
- Nikakhtar F., Ayromlou M., Baghran S., Rahvar S., Rahimi Tabar M. R., Sheth R. K., 2018, *Mon. Not. Roy. Astron. Soc.*, 478, 5296
- Peebles P. J. E., 1980, *The large-scale structure of the universe*
- Percival W. J., et al., 2010, *Monthly Notices of the Royal Astronomical Society*, 401, 2148
- Press W. H., Schechter P., 1974, *ApJ*, 187, 425
- Ramsundar B., Eastman P., Walters P., Pande V., 2019, *Deep learning for the life sciences: Applying deep learning to genomics, microscopy, drug discovery, and more*. O'Reilly
- Ravanbakhsh S., Oliva J., Fromenteau S., Price L. C., Ho S., Schneider J., Poczós B., 2017, *Estimating Cosmological Parameters from the Dark Matter Distribution* ([arXiv:1711.02033](https://arxiv.org/abs/1711.02033))
- Rhodes J., et al., 2019, *BAAS*, 51, 201
- Ribeiro M. T., Singh S., Guestrin C., 2016, "Why Should I Trust You?": Explaining the Predictions of Any Classifier ([arXiv:1602.04938](https://arxiv.org/abs/1602.04938))
- Sheth R. K., Tormen G., 1999, *Mon. Not. Roy. Astron. Soc.*, 308, 119
- Sheth R. K., Tormen G., 2002, *Mon. Not. Roy. Astron. Soc.*, 329, 61
- Sheth R. K., Mo H. J., Tormen G., 2001, *MNRAS*, 323, 1
- Siemiginowska A., et al., 2019, *Astro2020 Science White Paper: The Next Decade of Astroinformatics and Astrostatistics* ([arXiv:1903.06796](https://arxiv.org/abs/1903.06796))
- Springel V., Yoshida N., White S. D., 2001, *New Astronomy*, 6, 79
- Springel V., et al., 2005, *nature*, 435, 629
- Tinker J. L., Kravtsov A. V., Klypin A., Abazajian K., Warren M. S., Yepes G., Gottlober S., Holz D. E., 2008, *Astrophys. J.*, 688, 709
- Villaescusa-Navarro F., et al., 2021, *Multifield Cosmology with Artificial Intelligence* ([arXiv:2109.09747](https://arxiv.org/abs/2109.09747))
- White S. D. M., Rees M. J., 1978, *MNRAS*, 183, 341
- Yamashita R., Nishio M., Do R. K. G., Togashi K., 2018, *Insights into Imaging*, 9, 611
- Zhang Q., Wu Y. N., Zhu S.-C., 2018, *Interpretable Convolutional Neural Networks* ([arXiv:1710.00935](https://arxiv.org/abs/1710.00935))
- Zhang X., Wang Y., Zhang W., Sun Y., He S., Contardo G., Villaescusa-Navarro F., Ho S., 2019, *From Dark Matter to Galaxies with Convolutional Networks* ([arXiv:1902.05965](https://arxiv.org/abs/1902.05965))